Seventh International Conference on Computational Fluid Dynamics (ICCFD7), Big Island, Hawaii, July 9-13, 2012

ICCFD7-1004

High Resolution Finite Volume Scheme Based on Minimized Dispersion and Controllable Dissipation Reconstruction

Qiuju Wang*, Yuxin Ren* and Zhensheng Sun*
ryx@tsinghua.edu.cn

* Department of Engineering Mechanics, Tsinghua University, PR China.

Abstract: The minimized dispersion and controllable dissipation (MDCD) reconstruction technique optimizes dispersion and dissipation separately and shows desirable properties of both dispersion and dissipation. A low dispersion finite volume scheme based on MDCD reconstruction is proposed which is capable of handling flow discontinuities and resolving a broad range of length scales. Although the proposed scheme is formally second order of accuracy, the optimized dispersion and dissipation make it very accurate and robust so that the rich flow features and complex geometry encountered in many practical engineering applications can be handled properly. A number of test cases are computed to verify the performances of the proposed scheme.

Keywords: High Resolution, Reconstruction, Finite Volume Scheme.

1 Introduction

The low dispersion and dissipation schemes are required in the simulations of problems related to turbulence and computational aero-acoustics (CAA). The common feathers of these problems are the flow fields with a broad range of length scales. The optimized dispersion and dissipation are very important for a scheme to achieve high resolution so that the flow fields with rich flow features can be simulated with high accuracy in both amplitude and phase. It is recently recognized that the order of the truncation error of a numerical scheme only provides information on the asymptotic convergence rate to the exact solution without enough information on the actual error on a finite computational grid [1]. The formal order of accuracy is sufficient to indicate the performance of a scheme for longer wavelengths. However, the formal order of accuracy is not a good indicator for shorter waves relative to the grid size [2, 3].

S.K. Lele [4] presented a compact finite difference scheme with spectral-like resolution using Fourier analysis to quantify the phase errors of a scheme. Tam and Webb [5] devised the dispersion-relation-preserving (DRP) scheme to optimize coefficients to satisfactorily resolve short waves with respect to the computational grid. However, both the compact scheme and the DRP scheme are very difficult to obtain oscillation free numerical solutions if the flow fields contain shock waves and other discontinuities. Wang and Chen [6] optimized the candidate stencil of the upwind-biased WENO scheme of Jiang and Shu [7] in the wavenumber space, following the practice of the DRP scheme to achieve higher resolution for short waves with about 6 points per wavelength (PPW). Martin et.al [8] added an additional candidate stencils to obtain a set of symmetric candidates and used bandwidth optimization technique to determine the weights for the optimal stencil, maintaining a small amount of dissipation at high wavenumbers. In recognizing that the optimal dispersion should be minimal according to some chosen criteria while the optimal dissipation is often problem dependent, Sun et al [9] presented the minimized dispersion and controllable dissipation (MDCD) scheme by minimizing dispersion error and leaving one free parameter for adjusting dissipation. The optimized dispersion properties were not affected by the dissipation adjustment.

Most optimized schemes were designed in the framework of the finite difference methods. In comparison with the finite difference, the finite volume method (FVM) has several distinct advantages. The first one

is that the FVM is naturally conservative without spurious source/sink due to numerical treatment. The second one is that the FVM is particularly suitable for problems with shocks and other flow discontinuities. Furthermore, the FVM can offer an easier framework to handle the irregular geometry and moving boundaries. Therefore, it is important to study the FVM with optimized dissipation and dispersion properties. In the present paper, the MDCD technique is extended to the FVM. A distinct feature of the FVM is the solution procedure deals with the cell-averages rather than the point values of the dependent variables. Taking this fact into consideration, the MDCD reconstruction is proposed. This paper emphasize on the resolution rather than the formal accuracy of the FVM. Although the proposed scheme is formally second order of accurate, the optimized dispersion and dissipation make it very accurate and robust so that the rich flow features and complex geometry encountered in many practical engineering applications can be handled properly. Furthermore, the present MDCD reconstruction is similar in form to the MUCSL interpolation that is widely used in the FVM. This feature makes it readily to extend the MDCD reconstruction into multi-dimensional cases and multi-block grid arrangement. A number of test cases are computed to verify the performances of the proposed scheme.

2 Spatial discretization

We use the following scalar, one-dimensional linear advection equation to illustrate the development of the numerical procedures.

$$\frac{\partial u}{\partial t} + \frac{\partial f}{\partial x} = 0 \tag{1}$$

where $f = au$. The integration form of Eq. (1) in the control volume $I_j = [x_{j-1/2}, x_{j+1/2}]$ on uniform grids with spacing $(x_{j-1/2}, x_{j+1/2}) = h$ can be written as

$$\int_{x_{j-1/2}}^{x_{j+1/2}} (\frac{\partial u}{\partial t} + a\frac{\partial u}{\partial x})dx = \frac{\partial \bar{u}_j}{\partial t}h + (\hat{f}_{j+1/2} - \hat{f}_{j-1/2}) = 0 \tag{2}$$

where

$$\bar{u}_j = \frac{1}{h}\int_{x_{j-1/2}}^{x_{j+1/2}} u(x)dx \tag{3}$$

is the cell average of the dependent variable. The numerical flux function $\hat{f}_{j+1/2} = a\hat{u}_{j+1/2}$ For simplicity, we only considered the $a > 0$ case in which $\hat{u}_{j+1/2} = \hat{u}^L_{j+1/2}$, and $\hat{u}^L_{j+1/2}$ is computed by the reconstruction polynomial of cell I_j . The superscript "L" in $\hat{u}^L_{j+1/2}$ will be omitted hereafter for brevity. The $\hat{u}_{j+1/2}$ can be computed using a linear reconstruction denoted by

$$\hat{u}^{linear}_{j+1/2} = \sum_{\gamma=-(q-1)}^{q} a_\gamma \bar{u}_{j+\gamma} \tag{4}$$

where a_γ is the interpolation coefficient. It is apparent that the reconstruction is carried out on a stencil with is symmetric about the interface $(j + 1/2)$. There are $2q$ interpolation coefficients in Eq.(4) which are capable to reconstruct an unique $(2q-1)^{th}$-degree polynomial to achieve $2q^{th}$ order of accuracy for the interfacial state of the dependent variable. We consider the case $q = 3$, for which the interfacial state of the dependent variable in Eq.(4) can be computed by

$$\hat{u}^{linear}_{j+1/2} = (\alpha_{-2}\bar{u}_{j-2} + \alpha_{-1}\bar{u}_{j-1} + \alpha_0\bar{u}_j + \alpha_1\bar{u}_{j+1} + \alpha_2\bar{u}_{j+2} + \alpha_3\bar{u}_{j+3}) \tag{5}$$

The interfacial state $\hat{u}_{j+1/2}$ obtained from Eq. (5) is used to compute the numerical flux function:

$$\hat{f}_{j+1/2} = a\,(\alpha_{-2}\bar{u}_{j-2} + \alpha_{-1}\bar{u}_{j-1} + \alpha_0\bar{u}_j + \alpha_1\bar{u}_{j+1} + \alpha_2\bar{u}_{j+2} + \alpha_3\bar{u}_{j+3}) \tag{6}$$

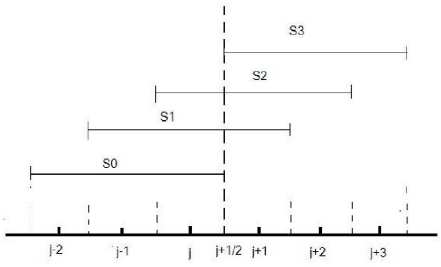

Figure 1: Symmetric stencil for $q = 3$ with 6 candidates.

According to the Lemma 1 of Ref.[9], in order to optimize the dispersion and dissipation separately, the reconstruction should be 4^{th} order although the highest possible order of accuracy is 6 for the case $q = 3$. Taylor series expansion of $\bar{u}_\beta$ to n^{th}-order of accuracy about interface $(j + 1/2)$ yields

$$\bar{u}_\beta = \frac{1}{h}\int_{x_{\beta-1/2}}^{x_{\beta+1/2}} u(x)dx = \frac{1}{h}\sum_{m=1}^{n}\left[\left(\frac{\partial^{m-1}u}{\partial x^{m-1}}\right)_{\beta+1/2}\frac{\left(x - x_{j+1/2}\right)^m}{m!}\Bigg|_{x_{j-1/2}}^{x_{j+1/2}}\right] \tag{7}$$

After substituting $\overline{u}_\beta(\beta = j - 2, ..., j + 3)$ into Eq.(6), it is straightforward to show that the following conditions ensure the 4^{th} order of accuracy of the reconstruction.

$$\alpha_{-1} = \frac{-1}{12} + \frac{-3}{2}\left(\alpha_{-2} + \alpha_3\right) + \frac{-5}{2}\left(\alpha_{-2} - \alpha_3\right) \tag{8}$$

$$\alpha_0 = \frac{7}{12} + \left(\alpha_{-2} + \alpha_3\right) + 5\left(\alpha_{-2} - \alpha_3\right) \tag{9}$$

$$\alpha_1 = \frac{7}{12} + \left(\alpha_{-2} + \alpha_3\right) - 5\left(\alpha_{-2} - \alpha_3\right) \tag{10}$$

$$\alpha_2 = \frac{-1}{12} + \frac{-3}{2}\left(\alpha_{-2} + \alpha_3\right) + \frac{5}{2}\left(\alpha_{-2} - \alpha_3\right) \tag{11}$$

Therefore, two more conditions are needed in order to uniquely determine the coefficients α_{-2} and α_3 , which will be provided by the MDCD optimization technique that will be presented in Section 3. After the optimization, the reconstruction will be called the (linear) MDCD reconstruction.

The linear reconstruction in Eq.(5) cannot be used directly to compute the flow fields with shock waves. In order to capture the shock waves, the nonlinear adaptation mechanism of the WENO scheme can be easily introduced. For the case $q = 3$, the interfacial state is computed by [8]

$$\hat{u}_{j+1/2}^{nonlinear} = \sum_{k=0}^{3}\omega_k u_{j+1/2}^k \tag{12}$$

where $u_{j+1/2}^k$ is obtained by a 2^{nd}-degree polynomial reconstructed on stencil S_k which, for $k = 0, 1, 2, 3$, is shown in Figure 1. The detailed formulation of $u_{j+1/2}^k$ is given by

$$u_{j+1/2}^0 = \frac{2}{6}\bar{u}_{j-2} + \frac{-7}{6}\bar{u}_{j-1} + \frac{11}{6}\bar{u}_j \tag{13}$$

$$u^1_{j+1/2} = \frac{-1}{6}\bar{u}_{j-1} + \frac{5}{6}\bar{u}_j + \frac{2}{6}\bar{u}_{j+1} \tag{14}$$

$$u^2_{j+1/2} = \frac{2}{6}\bar{u}_j + \frac{5}{6}\bar{u}_{j+1} + \frac{-1}{6}\bar{u}_{j+2} \tag{15}$$

$$u^3_{j+1/2} = \frac{11}{6}\bar{u}_{j+1} + \frac{-7}{6}\bar{u}_{j+2} + \frac{2}{6}\bar{u}_{j+3} \tag{16}$$

In Eq.(12), ω_k is the nonlinear weight associated with stencil S_k shown in Figure 1. According to Jiang and Shu [7], ω_k is computed by

$$\omega_k = \frac{\frac{C_k}{(\varepsilon+IS_k)^p}}{\sum_{k=0}^{3}\frac{C_k}{(\varepsilon+IS_k)^p}} \tag{17}$$

where C_k is the linear weight of the candidate stencil S_k , the constant ε is a small positive number to prevent division by zero, and p is chosen to be $p = 1$ to reduce the dissipation. It is evident that ω_k satisfies the condition:

$$\sum_{k=0}^{3}\omega_k = 1 \tag{18}$$

IS_k in Eq.(17) is the smoothness measurement which becomes larger when discontinuities are present within stencil S_k and remains relatively small otherwise. The definition of IS_k is presented by Jiang and Shu [7]. The smoothness IS_3 of purely downwind candidate S_3 is considered to satisfy

$$IS_3 = \max_{0\le k\le 3}(IS_k) \tag{19}$$

to prevent instability [8]. In the present paper, the weight functions of the WENO scheme will also be optimized by the MDCD technique. This procedure of optimization is different from that of [8] in the fact that the present procedure optimizes the dissipation and dispersion separately for a flexible control of the dissipation without affecting the optimized dispersion. However, it is difficult to optimize a non-linear scheme directly. Therefore, the linear counterpart of Eq.(12) obtained by setting $\omega_k = C_k$ will be used in the optimization procedure. The linearized scheme is identical to Eq.(5) if the coefficient C_k is given by

$$C_0 = \frac{3}{2}(\alpha_{-2} + \alpha_3) + \frac{3}{2}(\alpha_{-2} - \alpha_3) \tag{20}$$

$$C_1 = \frac{1}{2}\left[1 - 3(\alpha_{-2} + \alpha_3) + 9(\alpha_{-2} - \alpha_3)\right] \tag{21}$$

$$C_2 = \frac{1}{2}\left[1 - 3(\alpha_{-2} + \alpha_3) - 9(\alpha_{-2} - \alpha_3)\right] \tag{22}$$

$$C_3 = \frac{3}{2}(\alpha_{-2} + \alpha_3) - \frac{3}{2}(\alpha_{-2} - \alpha_3) \tag{23}$$

Therefore, the optimized WENO reconstruction can be deduced directly by the linear MDCD reconstruction. After the optimized values of α_{-2} and α_3 are obtained by the MDCD technique, $C_k(k = 0, 1, 2, 3)$ in Eq.(17) are computed by Eq.(20)$\sim$(23). The resulting reconstruction is called the MDCD-WENO reconstruction which is 4^{th} order accurate when the solution is smooth, and is capable of capturing flow discontinuities.

It has been observed that the nonlinear adaptation of the MDCD-WENO reconstruction may deterio-

rate the spectral properties of the schemes even in the smooth region [9]. To overcome these limitations, a hybrid scheme is presented by combining the linear part and the nonlinear part of reconstruction following the method of Ren et al.[10]. The advantage of the hybrid scheme is to retain the dissipation and dispersion properties of the linear reconstruction in most part of the solution domain whenever the solution is smooth and is capable of shock capturing. Furthermore, the hybrid reconstruction is more efficient than WENO reconstruction since the expensive non-oscillatory shock-capturing scheme is only used in the regions containing the discontinuities. The reconstruction of $\hat{u}_{j+1/2}^{hybrid}$ is carried out by

$$\hat{u}_{j+1/2}^{hybrid} = \sigma_{j+1/2}\hat{u}_{j+1/2}^{linear} + (1-\sigma_{j+1/2})\hat{u}_{j+1/2}^{nonlinear} \tag{24}$$

The factor $\sigma_{j+1/2}$ weights the linear optimal reconstruction in the smooth region over the shock capturing nonlinear reconstruction in the region containing discontinuities. The hybrid reconstruction can revert to the linear reconstruction when $\sigma_{j+1/2} = 1$ while to the nonlinear reconstruction when $\sigma_{j+1/2} = 0$. The weight is determined by a continuous function of the smooth indicator [10]

$$\sigma_{j+1/2} = \min\left(1, \frac{r_{j+1/2}}{r_c}\right) \tag{25}$$

where r_c is a threshold value chosen as 0.4 in the present paper. The smooth indicator $r_{j+1/2}$ is computed by

$$r_{j+1/2} = \min\left(r_j, r_{j+1}\right) \tag{26}$$

where

$$r_j = \frac{|2\Delta u_{j+1/2}\Delta u_{j-1/2}| + \varepsilon}{(\Delta u_{j+1/2})^2 + (\Delta u_{j-1/2})^2 + \varepsilon} \tag{27}$$

and $\Delta u_{j+1/2} = \bar{u}_{j+1} - \bar{u}_j$. The positive real number ε is defined by

$$\varepsilon = \frac{0.9r_c}{1-0.9r_c}\xi^2 \tag{28}$$

where the value of ξ is set to be 10^{-3}. The reconstruction given by Eq.(24) is called the MDCD-HY reconstruction hereafter.

3 Spectral properties optimization

In this process, the MDCD approach [9] will be used to achieve a separate optimization of the dissipation and dispersion properties of the finite volume scheme proposed in Section 2. Fourier analysis is used to optimize the spectral properties of the scheme, which will provided two more conditions that are needed in order to uniquely determine the coefficients α_{-2} and α_3 in Eq.(8)$\sim$(11).

3.1 Spectral properties

The Fourier analysis provides an effective way to quantify the resolution characteristics of the differencing approximation [4]. So it is used for spectral properties improvement. Consider a pure harmonic function

$$u = A(t)e^{ikx} \tag{29}$$

where x is position, k is wavenumber and $i = \sqrt{-1}$. The exact integration form of Eq.(1) in the control volume $\left[x_{j-1/2}, x_{j+1/2}\right]$ is

$$\frac{\partial \bar{u}_j}{\partial t}h + a\left(Ae^{ikx_{j+1/2}} - Ae^{ikx_{j-1/2}}\right) = 0 \tag{30}$$

while the approximate integration form of Eq.(1) in the the control volume $\left[x_{j-1/2}, x_{j+1/2}\right]$ is

$$\frac{\partial \bar{u}_j}{\partial t} h + \left(\hat{f}_{j+1/2} - \hat{f}_{j-1/2} \right) \tag{31}$$

where the average value in control volume is evaluated as

$$\bar{u}_j = \frac{1}{h} \int_{x_{j-1/2}}^{x_{j+1/2}} A e^{ikx} dx = \frac{A}{ikh} \left(e^{ikx_{j+1/2}} - e^{ikx_{j-1/2}} \right) \tag{32}$$

When all $\bar{u}_\beta \, (\beta = j-2, \cdots, j+3)$ in Eq.(32) are substituted into Eq.(6), the numerical flux is obtained as

$$\hat{f}_{j+1/2} = \frac{aA}{ikh} \sum_{p=-2}^{3} \alpha_p e^{-p(ikh)} \left(e^{ikx_{j+1/2}} - e^{ikx_{j-1/2}} \right) \tag{33}$$

Substituting Eq.(33) into Eq.(31) yields

$$\frac{\partial \bar{u}_j}{\partial t} h + aA \left(e^{ikx_{j+1/2}} - e^{ikx_{j-1/2}} \right) \left(\frac{\kappa'}{\kappa} \right) = 0 \tag{34}$$

where $\kappa' = k'h$ and $\kappa = kh$ are scaled wavenumbers. κ' is given by

$$\kappa' = -i \left[\begin{array}{l} -\alpha_{-2} e^{-3i\kappa} + (\alpha_{-2} - \alpha_{-1}) \, e^{-2i\kappa} + (\alpha_{-1} - \alpha_0) \, e^{-i\kappa} + \\ (\alpha_0 - \alpha_1) + (\alpha_1 - \alpha_2) \, e^{i\kappa} + (\alpha_2 - \alpha_3) \, e^{2i\kappa} + \alpha_3 e^{3i\kappa} \end{array} \right] \tag{35}$$

and κ' is defined as the modified wavenumber. The real part of κ', $\Re(\kappa')$, is associated with phase errors while the imaginary part $\Im(\kappa')$ is associated with the amplitude errors. $\Re(\kappa')$and $\Im(\kappa')$ can be written the following forms when Eq. (8)$\sim$(11) is used in Eq.(35):

$$\Re(\kappa') = \gamma_{disp} \sin 3\kappa - \left(4\gamma_{disp} + \frac{1}{6} \right) \sin 2\kappa + \left(5\gamma_{disp} + \frac{4}{3} \right) \sin \kappa \tag{36}$$

$$\Im(\kappa') = \left(\cos 3\kappa - 6 \cos 2\kappa + 15 \cos \kappa - 10 \right) \gamma_{diss} \tag{37}$$

where

$$\gamma_{disp} = \alpha_{-2} + \alpha_3; \quad \gamma_{diss} = \alpha_{-2} - \alpha_3$$

γ_{disp} in the real part $\Re(\kappa')$ is associated with dispersion while γ_{diss} in the imaginary part $\Im(\kappa')$ is associated with dissipation. Therefore, the dispersion and dissipation can be optimized separately since $(\alpha_{-2} + \alpha_3)$ and $(\alpha_{-2} + \alpha_3)$ are independent parameters.

3.2 Optimization of spectral properties

The dispersion is optimized by the minimization of the following objective function [9].

$$E = \frac{1}{e^{\nu\pi}} \int_0^\pi e^{\nu(\pi - \kappa)} \left(\Re(\kappa') - \kappa \right)^2 d\kappa \tag{38}$$

where the factor ν in the exponential term is used to control the error at small wavenumber. The optimized value γ_{disp} due to different ν shown in Table 1. In this paper γ_{disp} is chosen as

$$\gamma_{disp} = 0.0463783 \tag{39}$$

It is interesting to note that the results are identical to the results of [9] where the finite difference approach is used. However, the present results should be interpreted differently with that of [9] since the present coefficients are used to the cell-averaged values rather than the point values.

Table 1: optimal γ_{disp} due to different ν

ν	4	6	8	10
γ_{disp}	0.0714071	0.0545455	0.0463783	0.0420477

The amount of dissipation is determined by γ_{diss}. To ensure the stability of the scheme the dissipation should be non-negative for all wavenumbers. Therefore, the imaginary part of the modified wavenumber $\Im(\kappa')$ should be non-negative which results in

$$\gamma_{diss} \geq 0 \tag{40}$$

There is no systematic way to optimize the dissipation property of a scheme because of optimal dissipation may be problem dependent. A significant advantage of the MDCD reconstruction is that it provides the flexibility in adjusting the dissipation without corrupting its dispersion properties. In practice, we should choose dissipation as small as possible but large enough to ensure the stability of the simulation. This, in the present MDCD reconstruction, can be achieved by choosing a proper value of γ_{diss}.

The coefficients $\alpha_\gamma(\gamma = -2, -1, 0, 1, 2, 3)$ can be uniquely determined when γ_{disp} and γ_{diss} are specified, which are given by

$$\begin{aligned}
&\alpha_{-2} = \frac{1}{2}\left(\gamma_{disp} + \gamma_{disp}\right);\ \alpha_{-1} = \frac{-1}{12} - \frac{3}{2}\gamma_{disp} - \frac{5}{2}\gamma_{diss} \\
&\alpha_0 = \frac{7}{12} + \gamma_{disp} + 5\gamma_{diss}; \qquad \alpha_1 = \frac{7}{12} + \gamma_{disp} - 5\gamma_{diss} \\
&\alpha_2 = \frac{-1}{12} - \frac{3}{2}\gamma_{disp} + \frac{5}{2}\gamma_{diss}; \qquad \alpha_3 = \frac{1}{2}\left(\gamma_{disp} - \gamma_{disp}\right)
\end{aligned} \tag{41}$$

The coefficients $C_k(k = 0, 1, 2, 3)$ in Eq.(17) are then computed by Eq.(20)$\sim$(23).

The MDCD reconstructions, including the MDCD-WENO and MDCD-HY reconstructions can be easily extended into solving Euler and Navier-Stokes equations. In the present paper, the MDCD-WENO and MDCD-HY reconstructions have been applied in our in-house code RAIN3D, which is a 3D multi-block code solving steady and unsteady Navier-Stokes (including RANS) equations.

4 Numerical tests

In this section, a number of numerical tests are used to analyze the behavior of the MDCD-WENO and MDCD-HY reconstructions presented in Section 2 and Section 3. The numerical tests include the one dimensional problem of shock/entropy wave interaction, the tow-dimensional problem of right moving Mach 10 shock and three-dimensional problems of flows over an SD7003 airfoil and the DLR-F4 Wing-Body generic aircraft model.

4.1 Shu-Osher problem

The Shu-Osher problem represents a Mach 3 shock interacts with a density disturbance which was first proposed by Shu and Osher [11]. Its governing equations are the one-dimensional Euler equations and the initial non-dimensional flow conditions are

$$(\rho, u, p) = \begin{cases} (3.857143, 2.629369, 10333); & if(x < 1) \\ (1 + 0.2\sin(5x), 0, 1); & otherwise \end{cases} \tag{42}$$

The interaction between the shock and the density disturbance generates a flow field with both smooth structure and discontinuities. This is a good test case to evaluate the spectral properties as well as the shock-capturing capability of a scheme. The solution is advanced time up to $t = 1.8$ on the computational domain $x \in [0, 10]$. The CFL number is 0.2, which is low enough to ensure spatial discretization errors are dominant

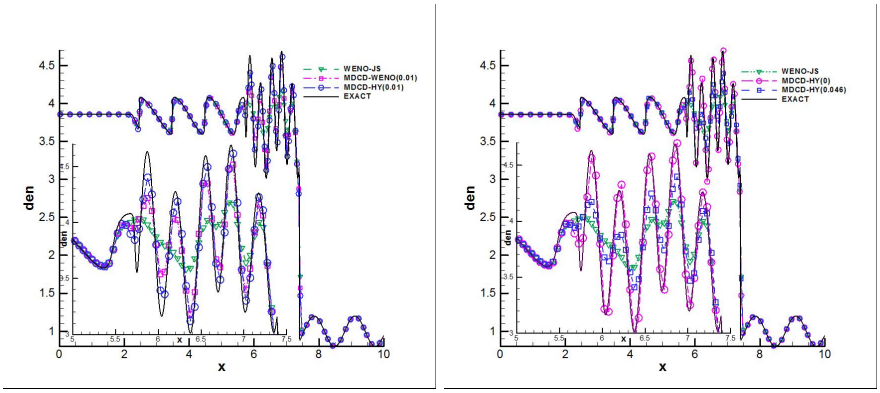

Figure 2: Shu-Osher problems. Distribution of density at $t = 1.8$ for MDCD-WENO,MDCD-HY and WENO-JS(left) and Distribution of density at $t = 1.8$ for MDCD-HY with different dissipations(right).

over time advancement errors. The grid number is $N = 200$. Density distributions are shown in Figure 2. For the case with $\gamma_{diss} = 0.01$, the results of the MDCD-WENO and the MDCD-HY reconstructions are labeled as MDCD-WENO(0.01) and MDCD-HY(0.01) respectively, and are shown in Figure 2. The "exact" solution is obtained by WENO-JS scheme [7] with the cell number $N = 2000$ although there is no real exact solution for the problem. As shown in Figure 2, the WENO-JS yields heavily damped solutions and both MDCD-HY and MDCD-WENO demonstrate superior resolution than WENO-JS in reproducing the correct flow structures downstream of the shock due to their better resolution. However, MDCD-WENO is more dissipative than MDCD-HY due to the over adaption of nonlinear weights in the smooth region. The comparison of MDCD-HY reconstruction with controllable dissipation coefficients $\gamma_{diss} = 0$ and $\gamma_{diss} = 0.046$ is shown in Figure 2. Even a small amount of dissipation will influence the results as shown in Figure 2. Therefore, the dissipation should be reduced as much as possible if it will not create spurious numerical oscillations. The flexibility of MDCD-HY reconstruction in adjusting the numerical dissipation is a great advantage for problems with both small scale structures and discontinuities.

4.2 Double Mach Reflection

This test case is a two dimensional test for high resolution schemes. The computational domain is defined as $(x, y) \in [0, 4] \times [0, 1]$ and a wall lies on the bottom of the computational domain starting from $x = 1/6$. The problem is about a right moving Mach 10 shock set up to makes an angle of with the $x - axis$ at $x = 1/6, y = 0$ and the initial non-dimensional flow conditions are

$$(\rho, u, v, p) = \begin{cases} (1.4, 0, 0, 1.0); & if(x > x_0 + y\sqrt{3}/3) \\ (8.0, 7.1447, -4.125, 116.5); & otherwise \end{cases} \tag{43}$$

where $x_0 = 1/6$. 800×200 cells are used in the computational domain and the solution is advanced time up to $t = 0.2$. The numerical results for MUSCL and characteristic-wise WENO-JS, MDCD-WENO(0.01), MDCD-HY(0.01) reconstructions are shown in Figure 3 and Figure 4.

The detailed discussion of the flow physics can be found in [12]. At the given output time two Mach stems form with two contact discontinuities. The second contact discontinuity, near the bottom of the wall, is extremely weak. The second Mach shock is rather weak and dies out entirely when it reaches the contact discontinuity from the first Mach reflection. This variation of the strength of the second Mach shock is very difficult to compute accurately. At the point where the first contact discontinuity approaches the reflecting wall the flow of the denser fluid is deflected by a pressure gradient built up in the region. Then a jet of the denser fluid is formed which shoots to the right along the wall [12].

As shown in Figure 3 and Figure 4, the main difference in the resolution of the contact discontinues and the associated jet is due to the dispersion and dissipation of the different reconstructions. Actually, the contact discontinuities are physically unstable structures of the flow. The converged numerical solution of the problem can be obtained when using the full viscous and heat conductive Navier-Stokes equations [13]. As

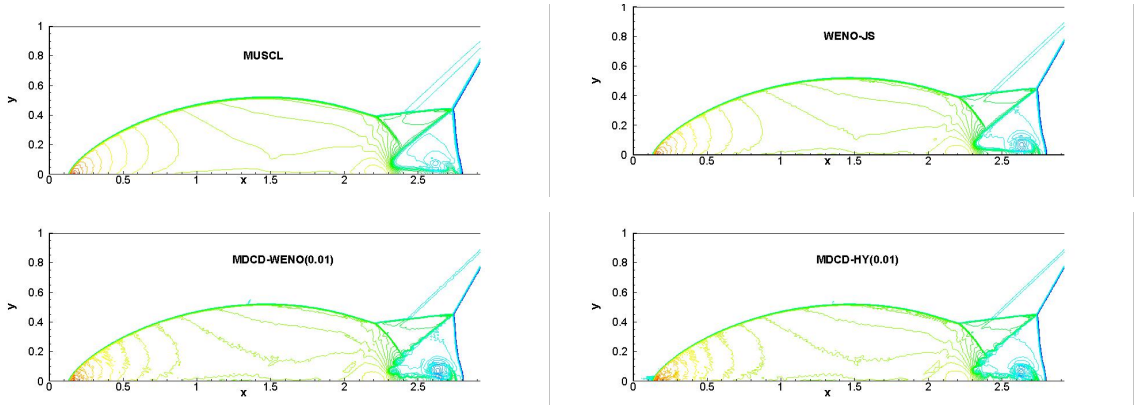

Figure 3: Density contours for double Mach reflection problem.

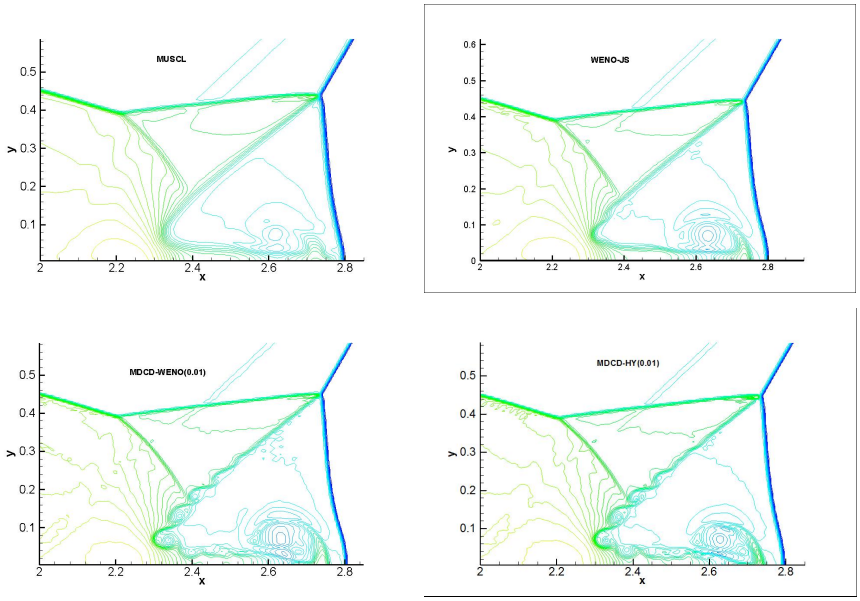

Figure 4: The enlarged portion of Figure 3.

for the Euler equations, the numerical dissipation is responsible for the viscosity and depends on the order of truncation error and spectral properties. Furthermore, no converged solution is obtained when mesh refined. Therefore the numerical schemes effect is the Kelvin-Helmholtz instability of the contact discontinuity and the instability is more pronounced, when the scheme is less dissipative. Therefore, The MDCD-WENO(0.01) and MDCD-HY(0.01) reconstructions with good spectral properties achievs higher resolution than the other two schemes and can capture the rollup structures of Kelvin-Helmholtz instability of the contact discontinuity more clearly.

4.3 Implicit Large Eddy Simulation of transitional flow over an SD7003 airfoil

The transitional flow over an SD7003 airfoil at low Reynolds number of 6×10^4 and the angle of attack of 4° degrees is characterized by the laminar separation bubbles (LSB), vortex breakdown, transition to turbulence and reattachment. Implicit Large Eddy Simulations using finite volume method with MDCD-HY(0.01) reconstruction is used to capture of the separation, transition process and reattachment process. The results show good agreement with experimental data and computations of high order schemes for separation, reattachment, and transition locations, as well as aerodynamic loads. The total grid number

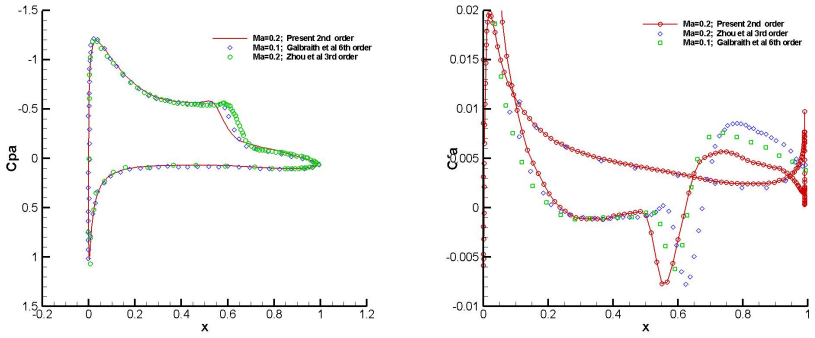

Figure 5: Mean pressure coefficient C_p (left) and mean skin friction coefficient C_f (right) on the wing surface with comparison to the computations by previously published results. Solid line: 2^{nd}-order FVM with MDCD-HY reconstruction; square symbols: Zhou et al [14]; diamond symbols: Galbraith et al [15].

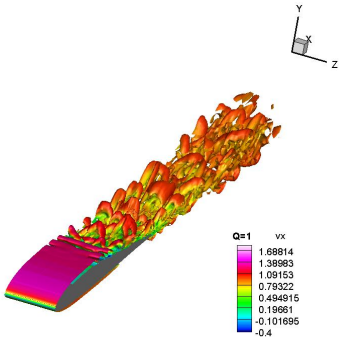

Figure 6: Instantaneous iso-surfaces of Q-criterion.

used present is 1,701,900. The test is computed at Mach number of 0.2.

The mean pressure coefficient and mean skin friction coefficient are compared to the results from Zhou et al [14] and Galbraith et al [15] in Figure 5. The results from Zhou et al [14] are computed by 3^{rd}-order spectral difference method with 2,119,500 degree-of-freedom and the results from Galbraith et al [15] are computed at Mach number of 0.1 by 6th-order on overset grid of approximately 5,700,000 grid points. Zhou et al [14] has verified that the Mach number of 0.2 is low enough for computations.

Although visible differences between different methods can be observed in Figure 5, the quantitative results presented in Table 2 show that the present results agree with the experimental results quite well. Table 2 compares locations of separation, transition, and reattachment from TU-SB and HFWT experimental data and computations with XFOIL [16], Zhou et al [14], *Galbraith et al*[1] [15] on overset mesh of of approximately 5,700,000 grid points and *Galbraith et al*[2] [15] on baseline mesh of $315 \times 151 \times 101$ grid points and the present ILES computation with a 2^{nd}-order finite volume method using MDCD-HY reconstruction. The computed separation location of the present ILES falls in between both experimental measurements. The present ILES computed transition location of 47% chord is in well agreement of the measured HFWT transition location and the Galbraith et al [15] transition location computed on baseline mesh. Reattachment locations are consistent between present ILES and TU-SB both at 62%. Instantaneous iso-surfaces of the Q-criterion are shown in Figure 6. A laminar separation bubble forms after the flow detaches from the suction side of the airfoil. As the vortex breakdown, a coherent spanwise vortex over the extent of the airfoil forms and subsequently breaks down into turbulent structure and reattaches to the wall.

Table 2: Separation, transition and reattachment locations

Case	FSTI [%]	Separation	Transition	Reattachment
Zhou et al	0	0.223	0.515	0.675
Galbraith et al[1]*(overset mesh)*	0	0.23	0.55	0.65
Galbraith et al[2]*(baseline mesh)*	0	0.24	0.45	0.61
Present	0	0.236	0.47	0.62
$TU-SB.exp$	0.08	0.30	0.53	0.62
$HFWT.exp$	∼0.1	0.18	0.47	0.58
$XFOIL$	0.07(N=9)	0.21	0.57	0.59

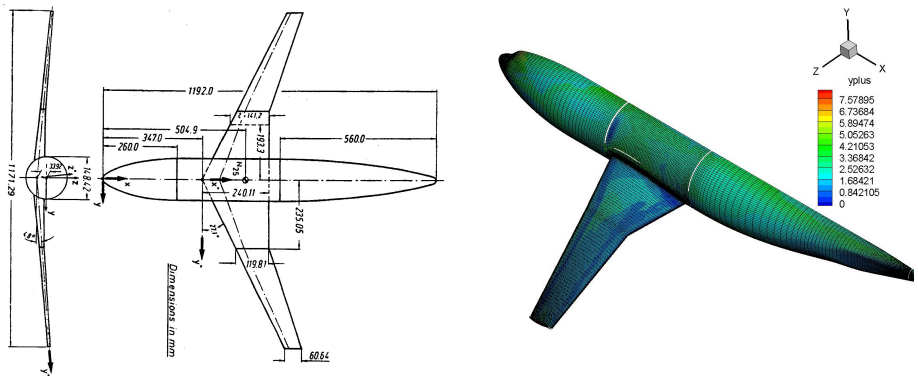

Figure 7: The DLR-F4 model (left) and Grid of the half model (right).

4.4 The DLR-F4 Wing-Body flows

The DLR-F4 Wing-Body generic aircraft model, depicted in Figure 7, has been selected as test case for the 1st AIAA Drag Prediction Workshop. The test cases are conducted to show the application of MDCD-WENO reconstruction to the complex aircraft configurations. The test conditions and reference quantities are listed in Table 3 and the test cases are listed in Table 4. There are 2,259,360 cells of the half model.

The MDCD-WENO reconstruction and the central scheme are used to compute the inviscid flux and the viscous flux respectively. The one-equation SA turbulence model by Spalart is selected as the turbulence model. In case 1, the integrated lift, drag and pitching moment perditions are compared to experimental data from Europe-an wind tunnels (NLR-HST, ONERA-S2MA, DRA-8ftąÁ8ft DRA Bedford [17]) and the simulation by Christopher Rumsey and Robert Biedron using CFL3D code [18] in Figure 8.

The simulations of MDCD-WENO reconstruction is on the 1-to1 grid of 2,259,360 cells while CFL3D are on the 1-to-1 grid of about 3.2 million cells. It is obvious that MDCD-WENO reconstruction is similar to CFL3D using "official" version S-A turbulence model in predicting the pitching moment while they are all similar in drag perdition. In case 2, pressure coefficient contour of the DLR-F4 wing/body configuration

Table 3: Test conditions and reference quantities

Testconditions	$Re = 3.0 \times 10^6, Ma = 0.75$
Wing ref. area	$S_{ref} = 0.1454m^2$
Aerodynamic mean chord	$C_{ref} = 0.1412m$
Aspect ratio	AR=9.5
Moment ref. center	$x = 0.5049, y = -0.03392, z = 0.$

Table 4: Test cases of DLR-F4 Wing-Body flows

Test cases	Test conditions
Case 1	$\alpha = \{-3°, -3°, -2°, -1°, 0°, 1°, 2°, 3°\}$ SA turbulence model
Case 2	$\alpha = -0.26°, CL = 0.5$ SA turbulence model

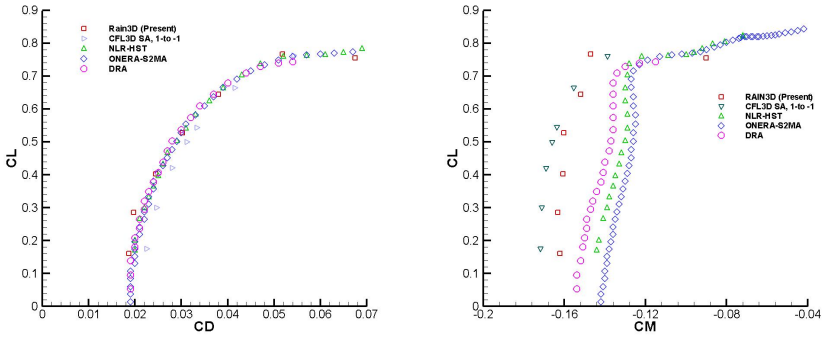

Figure 8: Integration of lift, drag (left) and pitching moment (right) coefficients.

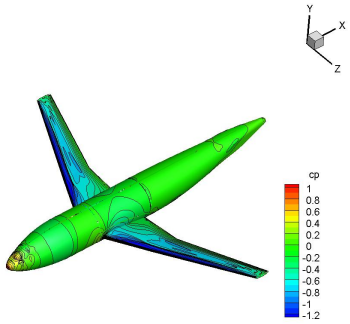

Figure 9: Pressure coefficient contour of the DLR-F4 Wing-body (CL=0.5).

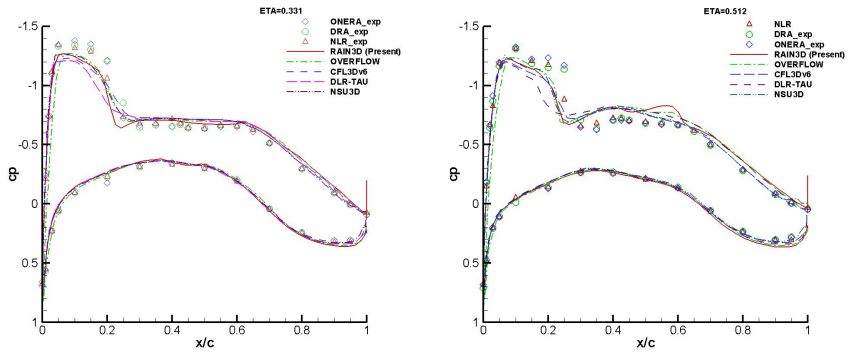

Figure 10: Chordwise pressure distributions at $eta = 0.331$ (left) and $eta = 0.512$ (right).

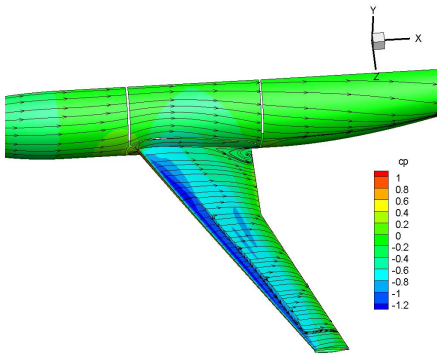

Figure 11: Streamlines and corner vortex.

Table 5: Grids and turbulence model of the flow solvers

Flow Solver	Structured grid	Unstructured grid	Turbulence model
Rain3D(Present)	2,259,360	–	S-A
CFL3Dv6	3.4×10^6	–	k-w SST
OVERFLOW	3,727,462(overset)	–	S-A
DLR-TAU	–	$2.36 \times 10^6((1 \times adapted))$	S-A;k-w
NSU3D	–	1.6×10^6	S-A

when CL=0.5 are shown in Figure 9.

The comparisons of chordwise pressure distribution at $eta = 0.331$ and $eta = 0.512$ are shown in Figure 10 in case 2. In Figure 10, the simulations of MDCD-WENO reconstruction using RAIN3D code are compared to the experimental data and other simulations which are computed by Robert Narducci [19] using CFL3Dv6 code, S. Melissa Rivers et al [20] using OVERFLOW code, Dieter Schwamborn and Mark Sutcliffe [21] using DLR TAU Code and David W. Levy [22] using NSU3D code. The details of compared simulations are listed in Table 5. Streamlines on the wing and the corner vortex (CL=0.5) are shown in Figure 11.

The DLR-F4 Wing/Body test case shows that the MDCD-WENO reconstruction can simulate the practical transonic flow over the complex configuration with shock boundary interaction and MDCD-WENO reconstruction shows comparable or better resolution than other codes with more grids.

5 Conclusion and Future Work

In this paper, the MDCD scheme with minimal dispersion and controllable dissipation is extended to the finite volume framework. Although the proposed scheme is formally second order of accuracy, the optimized dispersion and dissipation make it very accurate and robust so that the rich flow features and complex geometry encountered in many practical engineering applications can be handled properly. Several benchmark tests show excellent resolution of the MDCD-WENO and MDCD-HY reconstructions. Notable results include that the MDCD-HY reconstruction is successfully applied to the transitional flow simulation over an SD7003 airfoil characterized by the laminar separation bubbles (LSB), vortex breakdown, transition to turbulence and reattachment; and the MDCD-WENO reconstruction is applied to the practical transonic flow over the DLR-F4 Wing-Body configuration with shock boundary layer inter-action, and shows better resolution than other codes.

Acknowledgements: This work was supported by the National Natural Science Foundation of China (Grant Nos. 11172153 and 10932005).

References

[1] R. Vichnevetsky, J.B. Bowles, Fourier analysis of Numerical Approximations of Hyperbolic Equations. *SIAM, Philadelphia*, 1982

[2] W. Shyy, Computational Modeling for Fluid Flow and Interfacial Transport. *Elsevier, Amsterdam, the Netherlands*, 1994, Revised printing 1997.

[3] W. Shyy, A study of finite difference approximations to steady-state, convection-dominated flow problems. *Journal of Computational Physics*, 57:415-438, 1985

[4] S.K. Lele. Compact finite-difference schemes with spectral-like resolution. *Journal of Computational Physics*, 103(1):16-42, 1992

[5] C.K.W. Tam, J.C. Webb. Dispersion-relation-preserving finite difference schemes for computational acoustic. *Journal of Computational Physics*, 107:262-281, 1993.

[6] Z.J. Wang, R.F. Chen. Optimized weighted essentially nonoscillatory schemes for linear waves with discontinuity. *Journal of Computational Physics*, 174:381-404, 2001.

[7] G.S. Jiang and C.W. Shu, Efficient implementation of weighted ENO schemes.*Journal of Computational Physics*, 126:202-228, 1996.

[8] M.P. Martin, E.M. Taylor, M. Wu, V.G. Weirs. A bandwidth-optimized WENO Scheme for effective direct numerical simulation of compressible turbulence. *Journal of Computational Physics*, 220:270-289, 2006.

[9] Zhen-Sheng Sun,Yu-Xin Ren,Cĺędric Larricq,Shi-ying Zhang,Yue-cheng Yang. A class of finite difference schemes with low dispersion and controllable dissipation for DNS of compressible turbulence. *Journal of Computational Physics*, 230:4616-4635, 2011.

[10] Y.-X. Ren, M. Liu, H. Zhang, A characteristic-wise compact-WENO scheme for solving hyperbolic conservation laws. *Journal of Computational Physics*, 192:365-386, 2003.

[11] C.-W. Shu, S. Osher, Efficient implementation of essentially non-oscillatory shock-capturing schemes, ii, *Journal of Computational Physics*, 83:32-78, 1989.

[12] P. Woodward, P. Colella, The numerical simulation of two-dimensional fluid flow with strong shocks. *Journal of Computational Physics*, 54:115-173, 1984.

[13] Y.-T. Zhang, J. Shi, C.-W. Shu, Y. Zhou, Numerical viscosity and resolution of high-order weighted essentially nonoscillatory schemes for compressible flows with high Reynolds numbers, *Phys. Rev. E*, 68:1-16, 2003.

[14] Ying Zhou and Z.J. Wang, Implicit Large Eddy Simulation of Transitional Flow over a SD7003 Wing Using High-order Spectral Difference Method, *40th Fluid Dynamics Conference and Exhibit 28 June-1 July 2010, Chicago, Illinois*, AIAA-2010-4442, 2010.

[15] Galbraith, M. and Visbal, M., Implicit Large Eddy Simulation of low Reynolds number flow past the SD7003 airfoil, Proc. of the 46th AIAA Aerospace Sciences Meeting and Exhibit, Reno, Nevada, AIAA-2008-225, 2008.

[16] Drela, M., XFOIL Users Guide, Version 6.94 , MIT Aero. and Astro. Department, 2002.

[17] 1st AIAA CFD Drag Prediction Workshop. http://aaac.larc.nasa.gov/tsab/cfdlarc/aiaa-dpw/Workshop1, 2001.

[18] Christopher Rumsey, Robert Biedron, Drag Workshop Results Using CFL3D, 1st AIAA CFD Drag Prediction Workshop, June 9-10,2001, http://aaac.larc.nasa.gov/tsab/cfdlarc/aiaa-dpw/Workshop1/pdf/rumsey.pdf.

[19] Robert Narducci, AIAA Workshop Paper An Industry Application of CFL3D as a Transonic Drag Prediction Tool, 1st AIAA CFD Drag Prediction Workshop, June 9-10, 2001, http://aaac.larc.nasa.gov/tsab/cfdlarc/aiaa-dpw/Workshop1/pdf/narducci.pdf.

[20] S. Melissa Rivers, Pieter G. Buning, and Joseph H. Morrison, Investigation of an Overset Grid Flow Solver for Prediction of Subsonic Transport Cruise Performance, 1st AIAA CFD Drag Prediction Workshop, June 9-10, 2001. http://aaac.larc.nasa.gov/tsab/cfdlarc/aiaa-dpw/Workshop1/pdf/buing.pdf.

[21] Dieter Schwamborn and Mark Sutcliffe, Results obtained with the DLR TAU Code, 1st AIAA CFD Drag Prediction Workshop, June 9-10, 2001. http://aaac.larc.nasa.gov/tsab/cfdlarc/aiaa-dpw/Workshop1/pdf/lsutcliffe.pdf.

[22] David W. Levy, Use of NSU3D for Transonic Drag Prediction, 1st AIAA CFD Drag Prediction Workshop, June 9-10, 2001. http://aaac.larc.nasa.gov/tsab/cfdlarc/aiaa-dpw/Workshop1/pdf/levy.pdf.